Compensated Imaging over Arcminutes with Fringes in the Sodium Layer

Erez N. Ribak[1], Yael Baharav[2], and Joseph Shamir[2]
Department of Physics (1) and Department of Electrical Engineering (2),
Technion - Israel Institute of Technology, Haifa 32000, Israel

ABSTRACT

In order to increase the corrected field of view in multi-conjugate adaptive optics we suggest a method for measuring and separating the contribution of atmospheric turbulent layers[1,2]. The sodium layer serves as a huge screen, on which we project a wide fringe pattern from a single laser on the ground. A modified Hartmann-Shack sensor is employed to detect deformations in the pattern: sections of the fringe pattern are imaged by a lenslet array onto a large-format camera. Low layer turbulence causes overall shift of the fringe pattern in each lenslet, while high altitude turbulence results in internal deformations in the pattern, which are detected by that section of the camera which is behind each lenslet. Parallel Fourier analyses for the different lenslets allows separation of the atmospheric layers: the periodicity of the fringes lends itself to digital demodulation, which yields the deformations in the fringes. We present a statistical error analysis and simulations, showing good performance over a field of view of 80", compared to the performance expected of a conventional single sodium beacon, single adaptive mirror system.

1. INTRODUCTION

Conventional adaptive optics systems employing a single deformable mirror can only achieve a corrected field of view of the size of the isoplanatic angle. This is a serious drawback, especially when attempting to observe extended astronomical objects. A large number of deformable mirrors could provide phase compensation over wider field of view, but then one needs to measure the turbulence at different elevations. Using multiple guide stars at the sodium layer and below it, one can solve a set of equations for the phase gradient of the turbulent layers[3-9].

We propose a different approach[1,2] for multilayer wave front sensing which can provide turbulence information over a wide field of view. An almost perfect periodic pattern at the sodium layer as viewed through turbulence and telescope, has induced distortions which provide information on the atmospheric perturbations. To this end, we create a two dimensional periodic fringe pattern at

0-8194-1496-4/94/$6.00

the height of H=90–100 km, by interfering three parallel beams from a laser (Fig. 1). There is little distortion of the three beams, since they all emanate from within the lateral coherence area.

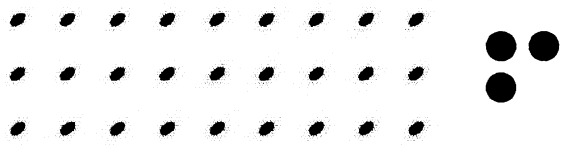

(a) (b)

Fig. 1. (a) A large part of the fringe pattern in the Na layer as viewed from the ground (simulation). The fringe spacing is 1÷5 m, and they cover an area of 45×45 m for a field of view of 1.3'. (b) The three up-going laser beams as viewed from above.

A lenslet array creates multiple images of the pattern on a large format camera. In each subaperture we produce a slightly different section of the fringe pattern, which had propagated along a slightly different atmospheric path on its way down. From this diversity in the imaged fringe patterns we extract the separate contributions to the wavefront aberrations. For ease of calculation, we treat the turbulence as if consisting of two parts – low and high altitude turbulent layers[1-4,10]. The bottom layer, below some boundary h_b, is represented by a phase screen at the telescope aperture, and the rest of the turbulence is represented by a phase screen at some height h_1 (fig. 2). Each layer is then conjugated to a separate deformable mirror.

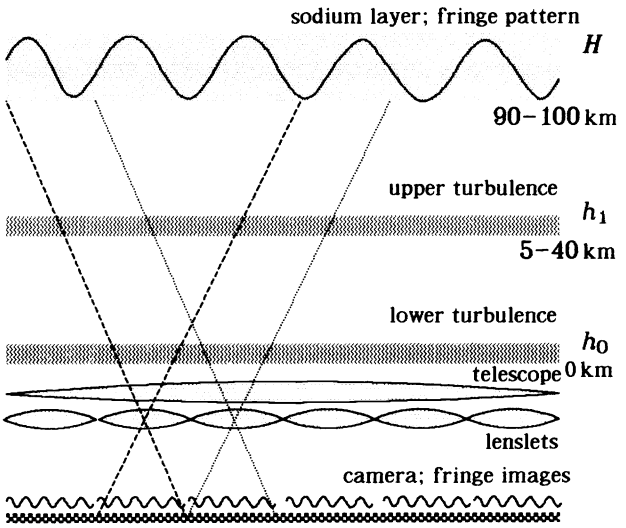

Fig. 2. The projected fringes in the sodium layer are imaged by the telescope and the conjugate lenslet array on a large-format camera. Here the atmosphere consists of two dominant turbulence layers. The fields of view of the lenslets (in broken and dotted lines) are partly overlapping at the higher layer.

2. FIELD OF VIEW AND PHASE SCREENS

The phase screen approximation enables us to determine the maximum possible compensated field of view: a turbulent layer can be represented by an equivalent phase screen without causing a bounded error within the required field of view. We require that (a) Diffraction within the layer is negli-

gible[3,8]; (b) A multi-conjugate adaptive mirror system corrects perfectly the measured errors (no errors due to the control system such as from lag between measurement and correction); and (c) The difference between the accumulated phases of two rays which had just crossed the turbulent layer is bounded. This is the main limitation of the proposed procedure: a turbulent layer is considered a phase screen only within a limited angle, which is a modified isoplanatic angle.

The modified isoplanatic angle[2] is defined for a single layer (rather than the whole atmosphere) as $\theta = [2.91k^2\int_{z_0}^{z_1} dz\,(z_{PS}-z)^{5/3}C_n^2(z)]^{-3/5}$, (Fig. 3) where $k=2\pi/\lambda$ is the wave number and C_n^2 is the refractive index structure constant. In the standard definition for the isoplanatic angle θ_{IP}, $z_0=z_{PS}=0$ and $z_1=\infty$. If we assume a two-layer atmosphere, then for the lower isoplanatic angle θ_0, $z_0=0$, $z_1=h_b$, and $h_0\equiv z_{PS}=0$ and for the higher isoplanatic angle θ_1, $z_0=h_b$, $z_1=\infty$, and $h_1\equiv z_{PS}$. The isoplanatic angles of the two layers can still add up to 1 radian if we require that the field of view ϕ is such that $\phi^{-5/3} = \theta_0^{-5/3} + \theta_1^{-5/3}$. We also find that $\theta_0>\theta_{IP}$ and $\theta_1>\theta_{IP}$ – both isoplanatic angles are larger than the total isoplanatic angle. Moreover, when the turbulence is layered or almost layered, $\phi>\theta_{IP}$: thinner layers lead to larger compensated field of view.

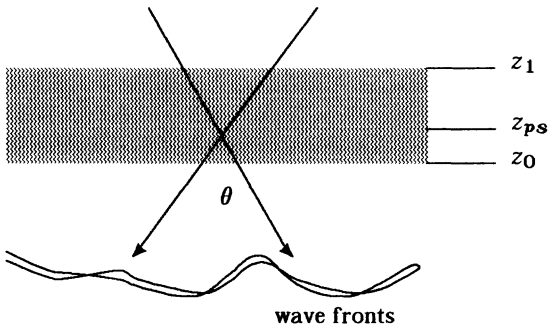

Fig. 3. Representing a turbulent layer between z_0 and z_1 by a phase screen at altitude z_{PS}. The isoplanatic angle θ is such that the variance of the difference between the resultant wave fronts deviates by one radian.

3. MEASURING TWO LAYERS

The fringe pattern is imaged by each lenslet in the array onto a different sub-detector. As in the standard Hartmann-Shack sensor, the bottom layer shifts the section of the pattern within the field of view of the lenslet. If $\rho_0 = [0.423k^2\int_0^{h_b} dz\,C_n^2(z)]^{-3/5}$ is Fried's parameter of the bottom layer, then we choose the diameter of the lenslet to be $d_0 < \rho_0$.

Each lenslet images part of the fringe pattern through a large section of the high layer (Fig. 2). Each point in the sodium layer is imaged through a slightly different section of the higher turbulence. Hence, a distortion of the fringe pattern is superposed on the shift induced by the bottom layer. We separate the contributions of the two layers by digital demodulation[11,12]. The fringe distortion (in one dimension, say the x direction; see full treatment in Ref. 2) is

$$I(x) = A\{1 + \cos[kx\Delta l/H + \Phi(x)]\}. \quad (1)$$

A the intensity of each of the interfering beams, Δl the distance between them, H the fringe height and Φ is the local phase (distortion) of the fringe period. This phase is not the actual phase of the wavefront, but its *gradient*, as in the conventional Hartmann-Shack sensor. Sampling and Fourier transforming, we get

$$i(p) = A\{\delta(p) + 0.5[\delta(p-\kappa)+\delta(p+\kappa)] * \mathbb{F}[e^{i\Phi(n)}]\} . \quad (2)$$

κ is the number of fringes across the field of view, which is adjusted optically to be an integer. $\mathbb{F}$ denotes Fourier transform, capital and small letters denote Fourier pairs of respective coordinates n and p. If there are L pixels facing a lenslet of diameter d_0, then the true phase gradient relates to the fringe distortion through $\Phi_g = L\Phi/d_0\kappa$.

Demodulation consists in shifting $i(p)$ by κ pixel, to center one of the side lobes, then saving only the information inside a window of size $L/3$. The average value around the origin is now $e^{i\bar{\Phi}}$, the tilt phasor produced by the lower layer. Transforming back only this window, the result is $e^{i\Phi(n)-\bar{\Phi}}$, the tilt phasor produced by the upper layer. The tilts in the lower layer can be found only up to $\bar{\Phi}$, their average value. There is an additional global tilt which has to be measured using a natural guide star. The procedure is repeated for both directions (x and y) and for all of the lenslets. The phase gradient maps of the upper phase screen are now shifted and added (Fig. 2). If α is the radius of the field of view of each lenslet (of diameter d_0), then the amount of shift is also d_0, the section size is $2\alpha h_1$ and the overlap is $d_0/2\alpha h_1$ at layer elevation h_1. The resolution at this layer is $6\alpha h_1/L$, which can be larger than the resolution at the bottom layer.

4. ERRORS

Poisson noise is significant in the visible regime; we deal with read-out and other additive noise sources separately[2]. If the average number of photons per pixel is $\bar{n}$, there are L^2 pixels, and the total intensity of the three beams is $3A$, then for each lenslet we have $\bar{N} = \bar{n}L^2 = 3AL^2$ photons. The photon flux density F (in photons/m^2) detected from the Na layer per laser pulse was calculated for the single guide star[13]. For the single star the number of photons per lenslet is $\bar{N} = Fd_0^2$ and for the fringe pattern $\bar{N} = Fd_0^2[2\alpha H/(D+2\alpha H)]^2$. We assume that the measurement error in the bottom and top layers are not correlated, so this sets a top limit to the errors. We also ignore the fact that the final phase map noise is different from the measured gradients because of averaging effects and because of noise propagation path.

We begin with the bottom layer. The phase error of each Fourier component[14,2] is $\sigma_\Phi \approx \sigma_I / H_R$. H_R is the real part of the component, and it depends on atmospheric properties; σ_I is the rms of the imaginary part, and it depends on photon noise[2]. The lower layer error is (e.g. in the x direction)

$$\sigma_{n0}^2 \approx \frac{3L^2}{4\kappa^2 \bar{N}} \frac{1}{\left[1-3.44\,(d_0/r_0)^{5/3}\,(\kappa/L)^2\right]^2} \,. \tag{3}$$

The top layer gradients are calculated by an inverse transform on the demodulated signal:

$$\sigma_{n1}^2 \approx \frac{d_1^2 L^4}{12 d_0^2 \kappa^2 \bar{N}} \frac{1}{\overline{M_x(\theta_x,\theta_y) M_y(\theta_x,\theta_y)}} \frac{1}{\left[1-3.44\,(d_0/r_0)^{5/3}\,(\kappa/L)^2\right]^2} \,, \tag{4}$$

where $\overline{M_x(\theta_x,\theta_y) M_y(\theta_x,\theta_y)}$ is the average number of lenslet images combined to achieve the phase gradient (see below) and θ_x, θ_y the direction of the astronomical object. d_0 is the dimension of the lenslets and of bottom mirror segments, and d_1 is the dimension of the top mirror segments (all square). For comparison, a single laser guide star system has a phase error of[15]

$$\sigma_n^2 = \frac{0.55\pi^2}{12\bar{N}} \,. \tag{5}$$

Linear fit error. The wave front phase variations inside each flat mirror segment are not possible to account for. We follow Fried[15], and find (numerically[2]) for each layer i the difference in a square aperture of side d_i and the layer Fried's parameter ρ_i

$$\sigma_{li}^2 = \frac{3.44\rho_i^{-5/3}}{d_i^4} \int_{-d/2}^{d/2}\int_{-d/2}^{d/2}\int_{-d/2}^{d/2}\int_{-d/2}^{d/2} dx\,dy\,ds\,dt \left\{1+\frac{12}{d_i^2}(xs+yt)\left[(x-s)^2+(y-t)^2\right]\right\}^{-5/6} . \tag{6}$$

Unisoplanatism error. The conventional single laser guide star system is limited by unisoplanatism, resulting from the different directions of the natural and artificial star, and by focal unisoplanatism, resulting from their different heights. By definition, $\sigma_{IP}^2 = (\theta/\theta_{IP})^{5/3}$: the error is 1 radian at the isoplanatic angle. Averaging over $\nu^2 = (D/d_0)^2$ apertures, we get

$$\sigma_{IP}^2 = \nu^{-2}\theta_{IP}^{-5/3} \sum_{n=1}^{\nu}\sum_{m=1}^{\nu} \left[(\theta_x - D/2h_1 + nd_0^2/h_1)^2 + (\theta_y - D/2h_1 + nd_0^2/h_1)^2\right]^{5/6} . \tag{7}$$

For the two layers we average over all angles in the field of view ϕ and get

$$\sigma_{IP0}^2 = \nu^{-2}\theta_0^{-5/3} \sum_{n=1}^{\nu}\sum_{m=1}^{\nu} \left[(\theta_x - \phi + 2n\phi/\kappa)^2 + (\theta_y - \phi + 2m\phi/\kappa)^2\right]^{5/6} , \tag{8}$$

$$\sigma_{IP1}^2 = \nu^{-2}\theta_1^{-5/3} \sum_{n_x=n_{ox}}^{n_{1x}} \sum_{n_y=n_{oy}}^{n_{oy}} M_x^{-1}M_y^{-1} \sum_{l_x=l_{ox}}^{l_{1x}} \sum_{l_y=l_{oy}}^{l_{1y}} [(\theta_x - 2l_x\phi/\kappa)^2 + (\theta_y - 2l_y\phi/\kappa)^2]^{5/6} . \quad (9)$$

The various summation indices n_x, n_y, l_x, l_y are limited by the pattern limits[2].

We add all the errors incoherently, assuming independence between them. For the single mirror, single star system we have $\sigma^2 = \sigma_n^2 + \sigma_l^2 + \sigma_{IP}^2$ and for our multiconjugate fringe system $\sigma^2 = \sigma_{n0}^2 + \sigma_{l0}^2 + \sigma_{IP0}^2 + \sigma_{n1}^2 + \sigma_{l1}^2 + \sigma_{IP1}^2$. Tables 1 and 2 show the parameters we used, and the results are given in Table 3 (for Profile 1), in Fig. 4 (Profile 1) and in Fig. 5 (all three profiles). We chose turbulence profiles and calculated Fried's parameter and the isoplanatic angles (Table 2). Profiles 1 and 2 are artificial profiles, described by six phase screens, with r_0 values of 0.4, 0.7, 1, 1.8, 2, 1.8 m. Profile 1 is of two thin turbulent layers, where we grouped the six phase screens at elevations of 0, 100, 200 m (bottom layer) and 9900, 10000, 10100 m (top layer). This profile was chosen to give realistic values of r_0 and θ_{IP}. Profile 2 is of two distinct but not thin turbulent layers, with phase screens at 0, 400, 800 m (bottom layer) and 9000, 10000, 11000 m (top layer). This profile was chosen so as to have an isoplanatic angle slightly larger than the field of view we aim to correct. Profile 3 is based on measured SCIDAR data[10] taken at a potential site for a telescope, and might not be representative or accurate. The C_N^2 profile is represented by 13 layers at elevations 50, 150, 250, 350, 450, 550, 650, and 750 m (bottom layer) and 8250, 9000, 10000, 11000, and 11750 m (top layer). The corresponding r_0 values of the phase screens are 0.2, 0.28, 0.43, 0.56, 0.68, 0.8, 0.91, 1.02, 3.18, 1.45, 1.16, 1.46 and 3.24 m. The isoplanatic angle of this distribution (Table 2) is too small for the attempted field of view, resulting in sub-optimal correction.

Table 1. Atmospheric and system parameters

T_A	Atmospheric transmission, one way	0.85	H	Na layer height	100 km
σ_s	Na backscatter cross section	$5.1{\cdot}10^{-16}$ m^2	η	Optical efficiency	0.075
C_s	Na column abundance	$5{\cdot}10^{13}$ m^{-2}	N_P	Laser pulses per second	100
D	Telescope diameter	5 m	d_0	Subaperture diameter	0.125 m
h_1	Phase screen height	10 km	κ	Fringes in lenslet FOV	20
ϕ	Radius of corrected field of view	40 arcsec	λ	Wavelength	$5.89{\cdot}10^{-7}$m
$L\times L$	Detector pixels per lenslet	100×100			

Table 2. Atmospheric turbulence profiles

	Profile:		1: thin	2:thick	3:La Silla
r_0	Fried's parameter	[m]	0.28	0.28	0.11
ρ_0	Bottom layer	[m]	0.3	0.3	0.12
ρ_1	Top layer	[m]	1	1	0.63
θ_{IP}	Isoplanatic angle	[arcsec]	6.2	6.2	3.9
θ_{IP1}	Bottom layer	[arcsec]	240	60	30
θ_{IP2}	Top layer	[arcsec]	830	83	44
ϕ	Isoplanatic FOV	[arcsec]	223	45	23

Table 3. Resulting errors for parameters given in Tables 1 and 2 for Profile 1. (in radians ; left value at center of field of view, right value at edge).

Error source	Bottom layer	Top layer	Conventional system
Poisson noise	0.1	0.13-0.18	0.20
Linear approximation	0.19	0.07	0.20
Unisoplanatism	0.19-0.26	0.10-0.08	0.71-4.35
Overall error	0.34-0.4		0.76-4.36

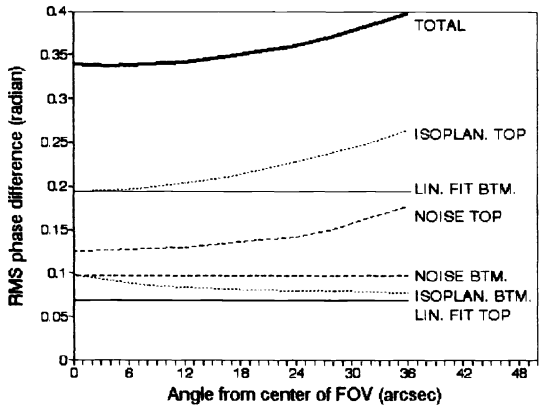

Fig. 4. Calculated error sources in correcting a perturbed phase front using the fringe pattern system for thin layers (Profile 1, Table 2). Errors are (by size): linear fit, top layer; unisoplanatism, bottom layer; Poisson noise, bottom; Poisson noise, top; linear fit, bottom; unisoplanatism, top; and sum of all errors.

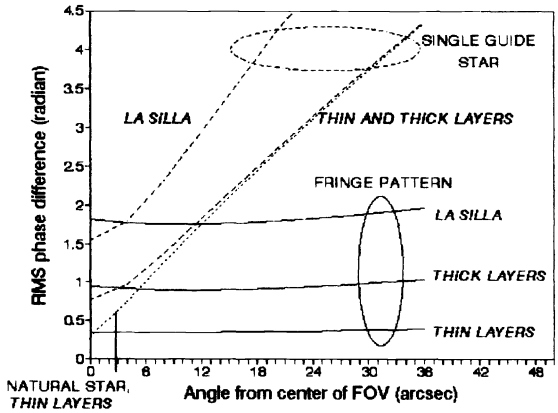

Fig. 5. Total error for the different systems and different turbulence profiles. Full line: fringe pattern system. Dashed: conventional single Na guide star system. Dotted: conventional single natural guide star system and thin layers (Profile 1, Table 2). The difference between it and the laser guide star (near the center) is because the latter causes a focal unisoplanatic error.

5. RESOURCES AND PERFORMANCE

The implementation of the fringe pattern system seems to be within current technology. We identify some limiting factors and some advantages of the system.

Detector. We divide the telescope aperture to $M \times M$ subapertures, and each images the fringes on $L \times L$ pixels. $D \approx 5$ m and $r_0 \approx 0.25$ m yield $M \approx 20$. Twenty to forty fringes in each subaperture imply[12] $N \approx 100$ pixels (see below). Thus we can use any combination between 400 cameras, each holding 10,000 pixels (one for each lenslet) and one large camera holding 4,000,000 pixels for the whole array. The frame read-out time (for both cases) depends on atmospheric conditions; 1 ms is a plausible time at the absence of prediction[18].

Computer. The method we propose (digital Fourier demodulation) requires a heavy computer system to take care of the processing load. Other methods such as detection of fringe maxima are possible, but we did not look into their requirements. We have (a) $M \times M$ Fourier transforms, each of size $L \times L$; (b) $2 \times M \times M$ demodulations (shift and apodize) in the x- and y-axis and $2 \times M \times M$ inverse transforms of size $L/3 \times L/3$; (c) Shifting and adding the $M \times M$ matrices. If we wish to end this process within one millisecond, current technology requires that the Fourier transforms are processed in parallel. Future products could make it even faster.

Laser. With the parameters in Table 1, the laser power[2] is 500 W (for Profile 3 slightly higher; for the single guide star 2.2 W;). These values are a function of the read-out noise (Fig. 6).

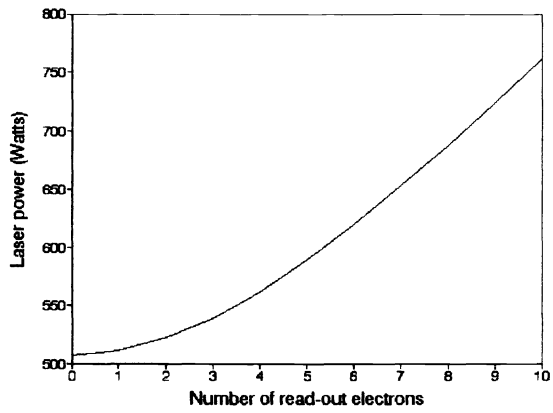

Fig. 6. Laser power needed to keep the total noise error is equal to 0.2 radian, as a function of detector read-out noise. The fringes cover 45 m and the field of view is 80". A copper vapor pumped dye laser can provide[17] 1000 W at the 589 nm. Forty percent less power is required if the sodium is not saturated[13] (cross section $\sigma_s = 8.27 \times 10^{-16}$ m^2).

Field of view. The diameter of the fringe pattern was limited arbitrarily to 45 m. Dividing by the elevation of the sodium layer (90 km) gives a cone of diameter 80 arcsec. A good correction within

this cone can be achieved provided that it is not larger than field of view, the latter being larger than the isoplanatic angle of the whole atmosphere, and even larger for thin atmospheric layers.

Lenslet and mirror element size. The subaperture size should be $d_0 \approx \rho_0$, which is larger than r_0 for the whole atmosphere. The mirror elements also follow this rule for the bottom layer and a similar one (with $d_1 \approx \rho_1$) for the top layer. The number of elements in both deformable mirrors will amount to less than twice the number of subapertures used in the single mirror method[5]. It is even smaller for small fields of view.

Distortion of up-going interference pattern. The distance between the beams is close to r_0, so they encounter almost the same turbulence on their way up. This effect causes a global tilt, common to all beams, and thus a uniform shift of the fringe pattern. This shift is cannot be detected by this or by other known laser guide star method, and must be measured independently. The use of natural guide stars for this purpose is enhanced because of the larger corrected field of view and thus the larger number of available stars within this field.

Location of emerging beams. The thickness of the sodium layer limits the fringe contrast. Since the angle subtended by the ascending rays is slightly different at each elevation in the sodium layer, the fringe spacing is slightly different. If the beams emerge from the center of the field of view (above the secondary of the telescope), than the aspect angles of the illumination and the observation are equal, and the contributions from the different layers add up in phase. If the beams are sent further off the telescope there is a gradual smearing of the fringes, reducing the contrast until full wash out.

Elevation of the top layer. By correlating the fringes from adjacent lenslets, it is possible to estimate the level of the top atmospheric layer. Hence the elevation to which the top mirror is to be conjugated is found directly, without reference to other techniques.

Partial correction of a wider field. One of the limiting factors in adaptive optics is the price and complexity of two flexible mirrors. The method we described permits the conjugation to the worse layer by a single mirror and correction of a wider field of view than the conventional method, which combines the contributions of all layers. The point spread function will be more even over a wider field. Also, if each lenslet images only one ρ_1 of the top layer then it is not possible (nor necessary) to correct this layer separately.

6. SIMULATION

One dimensional simulations of the system were compared to those of the conventional system, the latter having a narrower field of view, hence 1/4 the number of pixels. Atmospheric profiles were as in Profile 1 in Table 2 (details in Section 4). Poisson noise and diffraction effects were neglected. We used geometrical optics[3,4,8], and did not fit the gradient data to specific wave fronts (segmented mirrors were assumed). No prediction algorithms[18] were employed.

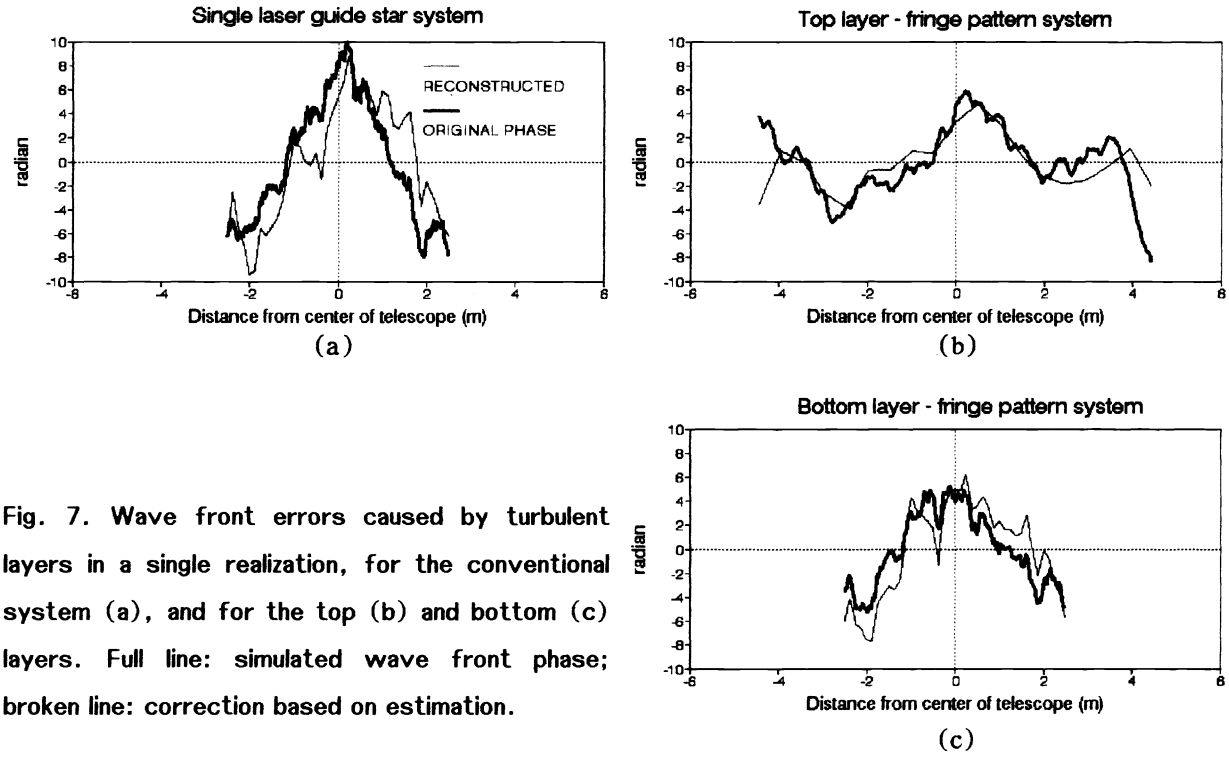

Fig. 7. Wave front errors caused by turbulent layers in a single realization, for the conventional system (a), and for the top (b) and bottom (c) layers. Full line: simulated wave front phase; broken line: correction based on estimation.

An example of a single realization is given in Fig. 7 and Fig. 8 (a). Fig. 8 (b) gives the average results over 100 realizations. Fig. 7(a) shows the phase shift caused by the whole atmosphere compared to the correction derived from the conventional system. The number of mirror segments is the same as the number of lenslets. The other panels show the phase shift caused by the two layers (for the same turbulence), compared to the two separate corrections derived by the system described in this paper. The number of bottom mirror segments is as in the conventional system. For the top layer less than half the number of correcting elements are used, even though the measurement is performed at a much higher resolution. The RMS optical path difference before and after the correction is shown in Fig. 8 as a function of angle from the center of the field of view. Fig. 8(a) gives the correction errors derived from the results given in Fig. 7 and (b) the

correction errors for an average over 100 different realizations. In all graphs (including the one depicted 'uncorrected') we assumed that the object star, at the center of the field of view, served for global tilt correction. In the case of thick layers (Fig. 8(c)) the system is not so efficient.

The simulation shows the advantage of the fringe system over the conventional system in the size of the corrected field of view. They are also in agreement with the numerical calculations in Section 4, although the absolute errors are larger because of unoptimized wave front fitting.

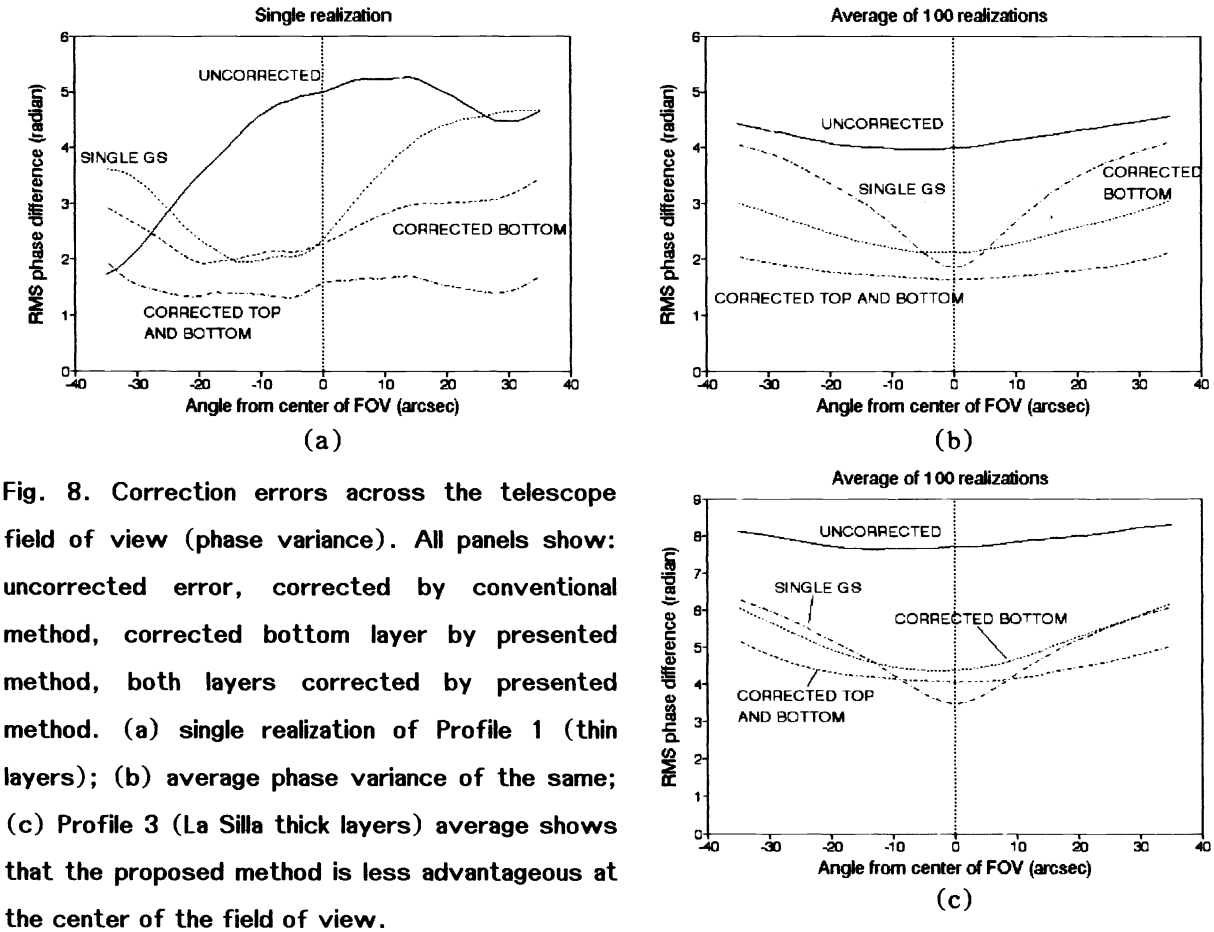

Fig. 8. Correction errors across the telescope field of view (phase variance). All panels show: uncorrected error, corrected by conventional method, corrected bottom layer by presented method, both layers corrected by presented method. (a) single realization of Profile 1 (thin layers); (b) average phase variance of the same; (c) Profile 3 (La Silla thick layers) average shows that the proposed method is less advantageous at the center of the field of view.

REFERENCES

1. Y. Baharav, E. Ribak, and J. Shamir, "Atmospheric tomography using a fringe pattern in the sodium layer". Optics Letters **19**, 242-244, 1994.
2. Y. Baharav, E. Ribak, and J. Shamir. "Interference fringes in the mesosphere for analysis of turbulence layers". Submitted, 1994.

3. M. Tallon, R. Foy, and J. Vernin " Wide field adaptive optics using an array of laser guide stars". Laser Guide Star Adaptive Optics Workshop, Albuquerque, NM, R. Q. Fugate, ed., 555-565, 1992.
4. M. Tallon and R. Foy, "Adaptive telescope with laser probe: isoplanatism and cone effect". Astronomy and Astrophysics **235**, 549-557, 1990.
5. J. M. Beckers, "Increasing the size of the isoplanatic patch with multiconjugate adaptive optics. pages 693-703. Proceedings ESO Conference #30, Very Large Telescopes and their Instrumentation, Garching, M.-H. Ulrich, Ed., 693-703, 1988.
6. D. L. Fried, "Evaluation of a concept for widening the useful field-of-view of an adaptive optics system". Optical Society of America Meeting, Maui Hawaii, 5-7, 1992.
7. D. Sandler, "A multiple spot laser beacon for high-order wavefront control: theory and experiment". Ref 3, 164-195, 1992.
8. J. Shamir, D. G. Crowe, and J. W. Beletic, "Improved compensation of atmospheric turbulence effects by multiple adaptive mirror systems". Applied Optics **32**, 4618-4628, 1993.
9. D. C. Johnston and B. M. Welsh, "Estimating the contribution of different parts of the atmosphere to optical wavefront aberration". Comp. Elec. Eng. **18**, 467- 484, 1992; "Analysis of a multiconjugate adaptive optics", J. Opt. Soc. Am. **A 11**, 394-408,1994.
10. M. Sarazin. Site testing for the VLT, VLT report no. 55. ESO Technical report, 1987.
11. C. Roddier and F. Roddier, "Interferogram analysis using Fourier transform techniques". Applied Optics **26**, 1668-1673, 1987.
12. S. Kostianovsky, S.G. Lipson, and E. N. Ribak, "Interference microscopy and Fourier analysis applied to measuring spatial refractive index distribution". Appl. Opt. **32**, 4744-4750,1993.
13. C. S. Gardner, B. M. Welsh, and L. A. Thompson, "Design and performance analysis of adaptive optical telescopes using laser guide stars". Proc. IEEE **78**, 1721-1743, 1990.
14. J. W. Goodman, *Statistical Optics*. John Wiley & Sons, 1985.
15. B. M. Welsh, "Performance analysis of adaptive-optics systems using laser guide stars and slope sensors". J. Opt. Soc. Am. A **6**, 1913-1923, 1989.
16. D. L. Fried, "Statistics of a geometric representation of wavefront distortion". J. Opt. Soc. Am. **55**, 1427-1435, 1965.
17. D. T. Gavel and J. R. Morris, "Sodium guide star adaptive optics system for astronomical imaging in the visible and near-infrared". Ref. 3, 619-628, 1992.
18. C.Schwartz, G. Baum, and E. Ribak, "Turbulence degraded wave fronts as fractal surfaces". J. Opt. Soc. Am. **A 11**, 444-451, 1994. "Fractal nature of atmospherically degraded wave fronts - an aid to prediction'', paper 2201-14, these Proceedings.